ORIGINAL PAPER

Flower-like WSe$_2$ used as bio-matrix in ultrasensitive label-free electrochemical immunosensor for human immunoglobulin G determination

Leijing Zhu[1] · **Jing Ma**[2] · **Danli Jin**[1] · **Yongjian Zhang**[1] · **Siyu Wu**[1] · **Ajing Xu**[2] · **Yingying Gu**[1] · **Yarui An**[1] · **Yuqing Miao**[1]

Abstract

The abnormal concentrations of human immunoglobulin G (hIgG) refers to many kinds of diseases. Analytical methods with the characteristics of rapid response, easy operation and high sensitivity should be designed to accurately determinate the hIgG levels in human serum. In this work, a label-free electrochemical immunosensor based on WSe$_2$/rGO was developed to sensitively detect human immunoglobulin G. First, the flower-like transition metal dichalcogenides (TMDCs) Tungsten Diselenide (WSe$_2$) with large effective specific surface area and porous structure was synthesized by hydrothermal synthesis. As a bio-matrix, the flower-like WSe$_2$ efficiently increased the active sites for loading antibodies. Meanwhile, reduced graphene oxide (rGO) obtained by tannic acid reduction was used to improve the current response of the sensing interface. WSe$_2$ was combined with rGO and the electrochemical active surface area (ECSA) of the sensing interface was enlarged to 2.1 times that of GCE. Finally, the combination of flower-like WSe$_2$ and rGO broadened the detection range and reduced the detection limit of the sensing platform. The immunosensor exhibited a high sensitivity with a wide linear range of 0.01–1000 ng/mL and low detection limit of 4.72 pg/mL. The real sample analysis of hIgG were conducted under optimal conditions, and the spiked recovery rates were between 95.5 and 104.1%. Moreover, satisfactory results were obtained by testing the stability, specificity and reproducibility of the immunosensor. Therefore, it can be concluded that the as-proposed immunosensor has the application potential of clinical analyze of hIgG in human serum.

Keywords Label-free immunosensor · WSe$_2$ · Transition metal dichalcogenides · Human immunoglobulin G

Introduction

Human immunoglobulin G (hIgG) is one of 5 isotypes of immunoglobulin (IgM, IgG, IgE, IgA and IgD). It plays a vital role in immune response by activating complements [1] and neutralizing various toxins [2]. The hIgG is the main component of antibodies in human serum and represents about 75% of all immunoglobulins [3], which is widely distributed in serum and non-mucosal tissues [4]. The concentration range of it is 7–16 mg/mL in healthy adult serum [5]. Abnormal hIgG levels are often associated with a variety of diseases such as cancers [6], liver diseases [7], systemic lupus erythematosus [8] and inflammatory bowel diseases [9]. Thus, the level of hIgG has been used as an index for diagnosis and predicting the prognosis of diseases. For example, the COVID-19 disease has threatened global public health in recent years. It was reported that high specific hIgG level was positively correlated with the severity of the disease at early stage [10]. Therefore, it is necessary for us to develop efficient methods to accurately measure the amount of hIgG in human body.

Various methods have been developed for sensitively analyzing hIgG, including immunofluorescence assay [11], lateral flow immunoassay (LFIA) [12], enzyme-linked immunosorbent assays (ELISA) [13], and electrochemiluminescence (ECL) immunoassay [14]. Satisfactory results were obtained in the detection of hIgG using the above methods,

Jing Ma: co-first author.

✉ Yarui An
anyarui@usst.edu.cn

1 Institute of Bismuth and Rhenium, School of Materials and Chemistry, University of Shanghai for Science and Technology, Shanghai 200093, China

2 Department of Pharmacy, Xinhua Hospital, School of Medicine, Shanghai Jiaotong University, 1665 Kongjiang Road, Shanghai 200092, China

there still exist some limits such as expensive instruments, long assay time, and complicated operating procedures. Among the numerous immunoassay methods, label-free electrochemical immunosensor is a promising method. It recognizes antigens by its corresponding antibodies that immobilized directly on the surface of sensing platform and monitors the concentration of the targets by measuring the electrochemical response. It has the superiorities of low cost, easy operation, rapid response, high sensitivity, and miniaturized equipment so that it has been widely applicated in the field of bioanalysis. Zhigang Yin et al. [15] developed a label-free electrochemical immunosensor based on PdPtCu@black phosphorus which took a short analysis time and achieved a low detection limit of 23 pg/mL. In consider of its merits, label-free electrochemical immunosensor is an appropriate choice for clinical assay of hIgG.

To enhance the sensitivity of the immunosensor, suitable materials should be exploited to raise the amounts of active sites on the sensing interface. Owing to the relatively high intrinsic hole mobility [16], sharp band edges [17] and strong light-matter interactions [18], two-dimensional transition metal dichalcogenides (TMDCs) have been a hot research topic in recent years. TMDCs have been extensively used in photocatalysis [19], field effect transistors [20], dye-sensitized solar cells [21], etc. There are many members of TMDCs, such as MoS_2, WS_2, $MoSe_2$ and WSe_2 as well. Benefit from its unique properties, Tungsten Diselenide (WSe_2) has become a hot issue in sensing technique fields. WSe_2 was used to construct field-effect transistor (FET) immunosensors and exhibited a moderate bandgap shows a high carrier mobilities [22]. Besides, profit from the high refractive index, WSe_2 was applied to increase the refractive index of plasma resonance biosensors [23]. What has activated our interest is that the surface activity and surface defects of WSe_2 could bind small molecules effectively on its surface, thus WSe_2 can be functionalized to load biological molecules. Hae Won Lee et al. [24] have reported that after O_2 plasma treatment, new binding sites of WSe_2 appeared, so that WSe_2 can combine more bioreceptors. In addition, in view of the large specific surface area, WSe_2 has been used to design the sensing interface to fix more biological macromolecules such as miRNA [25]. Harmanjit Kaur et al. [26] reported an aptasensor based on WSe_2 that functionalized by chitosan for bacterial toxin detection and showed a remarkable sensitivity.

Reduced graphene oxide (rGO) is a kind of two-dimensional carbon-based crystal materials. Many unique features of it were deeply studied. Firstly, owing to the removal of the oxygen-containing functional groups during reduction, rGO retains more aromatic (sp^2) domains than graphene oxide (GO), more electrons can move around in the entire plane layer, which could lead to the high conductivity [27]. Hence, metal oxides and transition metal dichalcogenides were

combine with rGO to overcome their poor conductivity [28]. Second, rGO has large aromatic plane and various functional groups, thus it can be utilized to bind biomolecules [29]. Third, the large specific surface area allows rGO to load other nanomaterials uniformly and prevent them from aggregation [30]. Besides, rGO can improve the sensitivity of the immunosensor by enlarging the active surface area of the sensing interface [31]. At last, it also owns advantages such as low cost and good biocompatibility [32]. Therefore, rGO is an ideal material for building sensing platforms.

In this study, we have fabricated a label-free electrochemical immunosensor for analyzing human immunoglobulin G. Firstly, the flower-like WSe_2 was obtained by hydrothermal synthesis. Numerous nanosheets of WSe_2 crossed to form a three-dimensional (3D) structure in which abundant pores were formed. As a result, the high specific surface area of WSe_2 acted as a bio-matrix for loading more antibodies. Then rGO was synthesized by an environmentally friendly process, using tannic acid (TA) as the reducing agent. The prepared rGO showed a chiffon-like morphology, and acted as a robust substrate to decorate WSe_2. The rGO enlarged the effective surface area of the sensing interface, vastly increasing the current response of the immunosensor. It may contribute to the magnification of the signals and the sensitivity of the immunosensor. As a result, with the combination of WSe_2 and rGO, the electrochemical active surface area (ECSA) of the sensing interface was enlarged. And satisfactory analytical performance of hIgG was achieved with the cooperation of WSe_2 and rGO. The developed label-free hIgG immunosensor exhibited an expanded liner range of 0.01–1000 ng/mL and an extremely low detection limit of 4.72 pg/mL under optimal conditions. More importantly, reliable results demonstrated the good capability of WSe_2 in improving the sensitivity of the sensing platform. The spiked recovery rate is between 95.5% and 104.1%, and the relative standard deviation is below 2.5%. Overall, the sensing platform we designed had revealed the feasibility of WSe_2 in establishing electrochemical immunosensor. The usage of WSe_2 also provided a helpful reference for later researchers and broadened the applications of TMDCs in the immunoassay field.

Experimental

Reagents and chemicals

Graphite powder, Concentrated sulfuric acid (H_2SO_4), Sodium nitrate ($NaNO_3$), Potassium permanganate ($KMnO_4$), 30% Hydrogen peroxide (H_2O_2), Sodium borohydride ($NaBH_4$), Chitosan, Bovine serum albumin (BSA), and Hydrochloric acid (HCl) were purchased from Sinopharm Group Chemical Reagent Co., Ltd. Sodium tungstate

(Na$_2$WO$_4$·2H$_2$O), Selenium powder, *N*, *N*-dimethylformamide (DMF), and Tannic acid (TA) were purchased from Shanghai Aladdin Biochemical Technology Co., Ltd. HIgG and hIgG antibodies were purchased from Beijing Dingguo Biochemical Reagents. Human immunoglobulin M (hIgM) was purchased from Sigma-Aldrich. Human IgG ELISA Kit was purchased from Hangzhou Lianke bio. All reagents are analytically pure. Ultrapure water was used in all experimental processes.

Apparatus and characterization

Scanning electron microscope (SEM) images were obtained from S-48000 scanning electron microscopy (Hitachi, Japan). Fourier transform infrared spectroscopy (FT-IR) spectra were recorded on a Thermo Nicolet 380 spectrometer. The X-ray diffraction (XRD) patterns were performed with an X-ray diffractometer (Bruker D8 Advance). Raman spectroscopy was conducted on a LabRAM HR Evolution (HORIBA). BET analysis was executed using a multi-channel automatic specific surface area analyzer (TriStarII3020, Mike Instruments). Ultrasound was operated on a Time ultrasound apparatus at room temperature with a power of 100 W. Electrochemical measurements, including cyclic voltammetry (CV), differential pulse voltammetry (DPV), and electrochemical impedance measurements (EIS) were performed on a CHI660E electrochemical workstation (Shanghai Chenhua Instrument Co., Ltd.).

Preparation of rGO

GO was synthesized by the modified Hummers method [33]. The synthesis process can be divided into three stages: low temperature, medium temperature, and high temperature. For the low temperature stage, 1 g graphite powder and 0.5 g sodium nitrate were dispersed in 23 mL concentrated sulfuric acid in an ice bath. Then, 3 g potassium permanganate was added into the beaker slowly with mechanical agitation, the black solution gradually became viscous. Sodium nitrate was used here to mitigate the severity of the reaction. Always pay attention to the temperature change, ensure the system temperature is below 5 °C. For the middle temperature stage, 46 mL deionized water was carefully poured into the above viscous material, followed by continuous stirring at 35 °C for 2 h. As the reaction progressed, the mixture gradually thickened, and the color gradually became brownish grey. In the final high temperature stage, 2.5 mL 30% H$_2$O$_2$ and 140 mL deionized water were introduced, and the temperature was raised up to 98 °C. After stirring for 1 h, bright yellow suspension was obtained and was static settled overnight to acquire the precipitation. The precipitate was washed to neutral with dilute hydrochloric acid and deionized water,

then was freeze-dried to obtain yellow sponge flocculent graphene oxide solid.

Reduced graphene oxide was reduced by tannic acid [34]. GO and tannic acid with a mass ratio of 1:4 was added into a certain volume of deionized aqueous solution, and was further ultrasonically dispersed. Then, the mixed solution reacted at 80 °C for 10 h. The product was centrifuged and was washed three times with deionized water and ethanol respectively. Finally, the product was freeze-dried to obtain a rGO flake solid. The preparation process was shown in Fig. 1A.

Preparation of chit-rGO

To disperse the prepared rGO equably and cover it on the GCE surface stably, chit-rGO was prepared. First, 0.5 g Chitosan was added to a mixed solution containing 1 mL Acetic acid and 99 mL pure water to prepared 0.5% Chitosan solution. Second, a certain amount of rGO powder was dissolved in 1 mL pure water containing 100 μL 0.5% Chitosan solution for immunosensor preparation.

Preparation of WSe₂

Flower-like WSe$_2$ was prepared by hydrothermal synthesis [35]. First, 0.64 g selenium powder and 0.2 g sodium borohydride were added to 60 mL DMF and stirred for two hours. Next, 1.32 g Na$_2$WO$_4$·2H$_2$O was introduced and stirred for another 1 h. The resulting solution was transferred to a 100 mL stainless steel autoclave and placed in an oven at 240 °C for 48 h. The obtained precipitate was washed three times with deionized water and absolute ethanol respectively. Finally, the washed precipitate was dried in an oven to obtain WSe$_2$ powder. At last, 1 mg WSe$_2$ was dissolved in 1 mL pure water to prepare the solution (1 mg/mL) for sensing platform preparation. The process was shown in Fig. 1B.

Fabrication of immunosensor

The preparation process of the immunosensor is shown in Fig. 1C. Firstly, the bare glassy carbon electrode (GCE, diameter 3 mm) was polished on the flannel with alumina powder of size 1, 0.3, 0.05 μm respectively, follow by continuously sonicating with deionized water and absolute ethanol for 5 min, and was then naturally dried in a ventilated place at room temperature. Secondly, 3 μL chit-rGO was dropped on the bare GCE and was dried completely at room temperature. Then 3 μL WSe$_2$ (1 mg/mL) was casted to get WSe$_2$/rGO/GCE. Next, 5 μL anti-human IgG (Ab) was incubated for 12 h in a refrigerator at 4 °C. After incubation, the Ab/WSe$_2$/rGO/GCE was carefully rinsed off with phosphate buffer solution (pH = 7.0, PBS) to wipe off the uncombined antibodies. Afterwards, 5 μL bovine serum albumin (BSA)

Fig. 1 Preparation process of rGO (**A**), flower-like WSe₂ (**B**) and fabrication procedure of the immunosensor (**C**)
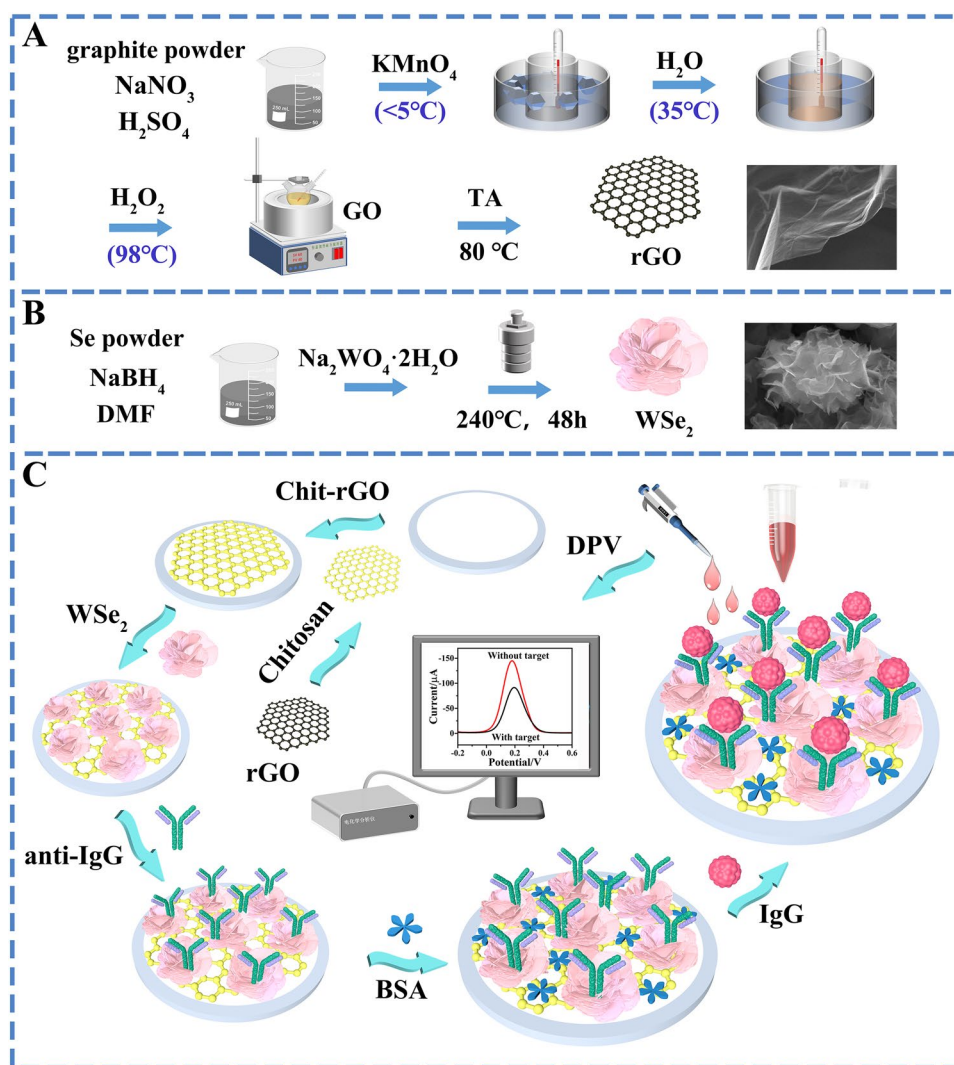
solution (1%, w/v) was dropped and incubated at 4 °C for 1 h to block non-specific binding sites. Next, the BSA/Ab/WSe₂/rGO/GCE was soaked in a series of hIgG solutions of different concentrations and incubated at 37 °C for 1 h. The unbound antigens were washed away with PBS. Finally, the prepared electrochemical immunosensors were successfully prepared for further tests.

Electrochemical measurements

All electrochemical measurements were operated using conventional three-electrode system: the glassy carbon electrode (GCE, 3 mm diameter) as the working electrode, the platinum wire electrode as the counter electrode, and the saturated calomel electrode as the reference electrode. The electrochemical measurements were performed by the electrochemical workstation model CHI660E in phosphate buffer solution (pH = 7.0, PBS) containing 2.5 mM $[Fe(CN)_6]^{3-/4-}$ and 0.1 M KCl. The potential range selected

for cyclic voltammetry (CV) and differential pulse voltammetry (DPV) was -0.2–0.6 V. The parameters selected for electrochemical impedance (EIS) measurement were alternating voltage of 5 mV and frequency range 10^{-2}–10^5 Hz. All potential sweeps were from negative potential to positive potential.

Results

Characterisation of rGO

To fully prove the successful preparation of the rGO, SEM, XRD, FTIR and Raman spectroscopy were applied. Figure 2A is the overall SEM image of rGO, the characteristic wrinkle morphology of graphene can be observed. Each layer is extremely thin, and accumulations rarely occur. The partially magnified SEM image of rGO was exhibited in Fig. 2B, the rGO shows a chiffon-like morphology.
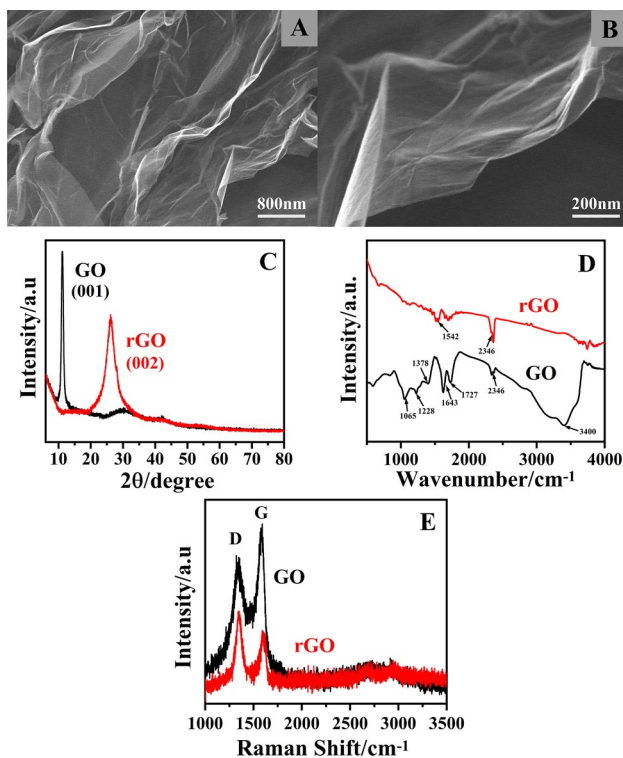
Fig. 2 The overall (**A**) and partially magnified (**B**) SEM image, XRD patterns (**C**), FTIR spectrum (**D**), and Raman spectrum of rGO (**E**)

Therefore, the rGO with large surface size could provide large amounts of active sites to facilitate the fixation of WSe$_2$. Figure 2C is the XRD pattern before and after the reduction of GO. It is obviously to found that the diffraction peak at $2\theta = 11°$ corresponds to the (001) crystal plane of GO, and the interplanar spacing is 0.80 nm. In the pattern of rGO, the diffraction peak at 11° basically disappears while a new peak appears at $2\theta = 26°$. This peak corresponds to the (002) crystal plane of graphene, and the interplanar spacing is about 0.342 nm, which is close to the standard graphene with a interplanar spacing of 0.335 nm [34].

GO has a great number of functional groups such as carboxyl groups, hydroxyl groups and carbonyl groups which belong to aliphatic (sp^3) domains, while the rest of the area of aromatic (sp^2) dominate less [27]. As for rGO, most oxygen-containing functional groups were chemically reduced by tannic acid, thus more aromatic (sp^2) domains of rGO were retained. Hence, FT-IR was used to characterize the changes of groups before and after the reduction of graphene oxide. The peak at 2346 cm^{-1} of the two curves in Fig. 2D were caused by the absorption of CO$_2$ in the air. It can be observed that there is a wide strong peak at 3400 cm^{-1} and a narrow peak at 1378 cm^{-1} in GO, which correspond to the tensile vibration and bending vibration of –OH, respectively. Two peaks at 1065 cm^{-1} and 1228 cm^{-1} refer to the vibration of the –CO bond in epoxy and alkoxy groups. The

tensile vibration of the carbonyl group (–C=O) appeared at 1727 cm^{-1}. And the peak at 1643 cm^{-1} belongs to the vibration of the carbon skeleton in the unoxidized graphite region. The intensity of the oxygen-containing peak at the corresponding position in rGO reduced significantly, and even some of the oxygen-containing peaks disappeared, indicating that large number of oxygen-containing groups were removed. In addition, the FT-IR spectrum of rGO shows a new C=C bond vibration peak at 1542 cm^{-1} [36]. The variation of these peaks firmly indicated that GO was successfully reduced to rGO.

Raman spectroscopy was used to further analyze the structure of rGO. As shown in Fig. 2E, two strong diffraction peaks located at approximately 1350 cm^{-1} and 1585 cm^{-1}. The former peak position represents D-band, which is generally related to internal structural defects, edge defects, and dangling bonds. The latter is the G band that represents the degree of sp^2 hybridization of carbon atoms in graphite materials [37]. Generally, whether the GO was reduced is determined by the increase of the D peak intensity relative to the G peak (I_D/I_G). The I_D/I_G ratio of GO and rGO is 0.85 and 1.27, respectively. The I_D/I_G ratio of rGO increased significantly, indicating that GO was reduced by tannic acid.

Characterisation of WSe$_2$

The overall and the partially magnified SEM image of WSe$_2$ were shown in Fig. 3A, B, respectively. As is shown in Fig. 3B, the nanosheets of WSe$_2$ crossed to form a three-dimensional flower-like structure, with each "petal" being an ultra-thin nanosheet. Meanwhile, it can be observed that the interlacing of the WSe$_2$ nanosheets formed numerous gaps and resulted in the porous structure. The three-dimensional structure of WSe$_2$ increased the number of nanosheets per unit area, thus it can provide more active site to load antibodies. As a bio-matrix, the flower-like WSe$_2$ increased the number of antigen–antibody complexes on the sensing interface and improved the detection range and sensitivity of the immunosensor.

The energy spectrum (EDS) of WSe$_2$ is shown in Fig. 3C. It can be observed that the synthesised material contains elements of W and Se, and the atomic content ratio of Se and *W* is 1.9, which is extremely close to the theoretical stoichiometry of WSe$_2$. The result determined that the WSe$_2$ was successfully synthesized.

The porous structure of flower-like WSe$_2$ was analyzed by BET. In Fig. 3D, the nitrogen adsorption–desorption curve shows a significant hysteresis loop at higher P/P_0, which is a typical IV isotherm, indicating that the synthesised WSe$_2$ possess a mesoporous structure. BET test results verified that the flower-like WSe$_2$ were formed by interlacing of nanosheets, and the pores were the gaps that formed between nanosheets which corresponded to the SEM result

Fig. 3 The overall (**A**) and partially magnified (**B**) SEM image, energy spectrum (**C**), and isotherm of N$_2$ adsorption and desorption of WSe$_2$ (**D**)
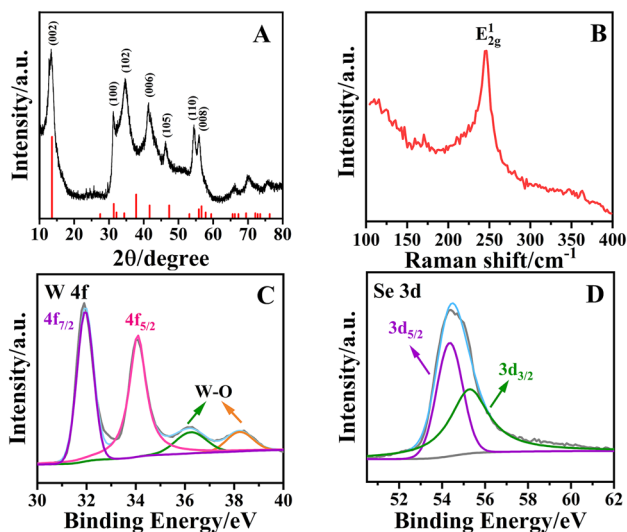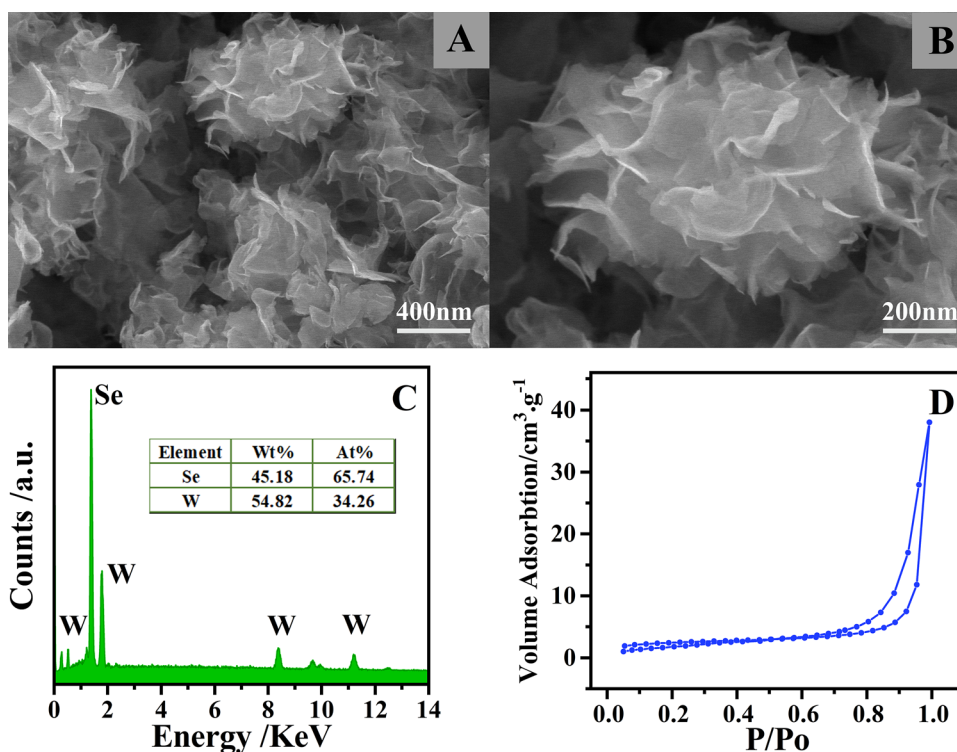

Fig. 4 The XRD pattern (**A**), Raman spectrum (**B**), W 4f XPS spectra (**C**) and Se 3d XPS spectra (**D**) of WSe$_2$

in Fig. 3A, B. Benefit from the unique flower-like three-dimensional porous structure, the active of the sensing interface can be ameliorate, so that more antibodies can be loaded onto WSe$_2$.

Figure 4A is the XRD pattern of WSe$_2$. Most of the diffraction peaks are consistent with the standard card of hexagonal structure WSe$_2$ (JCPDS card number 38–1388).

The diffraction peaks of Bragg angle (2θ) at 13.27°, 31.59°, 34.37°, 41.54°, 46.08°, 54.57°, 66.18° corresponded to (002), (100), (102), (006), (105), (110), (108) plane, respectively. The XRD pattern firmly verified that the WSe$_2$ was formed. Figure 4B is the Raman spectrum of WSe$_2$. An obvious characteristic peak of WSe$_2$ that appeared at ~249 cm^{-1} is assigned to the E$^1_{2g}$ (in plane). The A$_{1g}$ (out-of-plane) mode is not obvious here due to the relatively low peak intensity and small energy difference compared with E$^1_{2g}$. [38, 39]. Therefore, Raman spectrum further proved the successfully synthesis of WSe$_2$. To analyze the valence states of elements of WSe$_2$, the high-resolution XPS spectrums were recorded in Fig. 4C and D. Two peaks at 31.94 and 34.08 eV were attributed to W 4f$_{7/2}$ and W 4f$_{5/2}$ respectively, which represented the +4 state of W [35, 40]. Meanwhile, two small peaks at 36.24 and 38.22 eV were ascribed to the characteristic of W–O bond [35, 40]. In Fig. 4D, the peak of Se 3d was deconvolved into two peaks at 54.35 and 55.27 eV, which were attributed to Se 3d$_{5/2}$ and Se 3d$_{3/2}$, verifying the existing of Se^{2-} in WSe$_2$ [35, 38]. Therefore, the above results confirmed the preparation of WSe$_2$.

Electrochemical properties of the sensing interface

As the ion diffusion on the sensing interface will greatly affect the performance of the immunosensor, it is of vital importance to characterize its electrochemical properties.

The CV curves of the immunosensor (WSe$_2$/rGO/GCE) were recorded at different scan rate from 0.02 to 0.7 V/s in a phosphate buffer solution (PBS, pH = 7.0) which contains 2.5 mM [Fe(CN)$_6$]$^{3-/4-}$ and 0.1 M KCl. As displayed in Fig. 5A, the peak current increased as the scan rate increased. In Fig. 5B, the relevant linear regression equation of the anode is $I_{pa}(\mu A) = -295.1v^{1/2} - 6.705(R^2 = 0.9982)$, and the cathode is $I_{pc}(\mu A) = 337.1v^{1/2} + 5.698(R^2 = 0.9969)$. Both anodic peak current I_{pa} and cathodic peak current I_{pc} demonstrated a linear relationship with the square root of the scanning rate respectively, indicating that the oxidation–reduction reaction at the interface of the sensing interface was a diffusion-controlled process [41].

Chronocoulometry test

To demonstrate the effect of WSe$_2$ and rGO on improving the electrochemical active surface area and explore the effective specific surface area of the electrochemical immunosensor (WSe$_2$/rGO/GCE), chronocoulometry was performed in PBS (pH = 7.0) containing 2.5 mM [Fe(CN)$_6$]$^{3-/4-}$ and 0.1 M KCl. Meanwhile, we calculated the effective specific surface area (A_{eff}, cm^2) by Anson Eq. (1) [42]:

$$Q = \frac{(2nFAcD^{1/2}t^{1/2})}{\pi^{1/2}} + Q_{\text{dl}} + Q_{\text{ads}} \tag{1}$$

where Q (C) refers to charge, n ($n = 1$) is the number of the transferred electrons, F (96,500 C/mol) is Faraday's constant, c (2.5 mmol/dm^3) is substrate concentration, D (cm^2/s) is diffusion coefficient (7.60×10^{-6} cm^2/s, 25℃), and t (s) is electrolysis time, Q_{dl} (C) refers to the double-layer charge and Q_{ads} (C) is the adsorbed charge. Figure 6A is Q-t plot of two different platforms, curve a represents to GCE, b is WSe$_2$/rGO/GCE. While the linear equations in Fig. 6B were $Q_a(mC) = 0.05763t^{1/2} + 0.02286(R^2 = 0.9988)$, $Q_b(mC) = 0.1227t^{1/2} + 0.05773(R^2 = 0.9968)$, respectively. The values of A_{eff} according to the slopes in Q-$t^{1/2}$ graphs were obtained as 0.077 cm^2 and 0.16 cm^2, respectively. The WSe$_2$/rGO/GCE platform showed a larger effective specific surface area, which is 2.1 times in GCE. In a word,
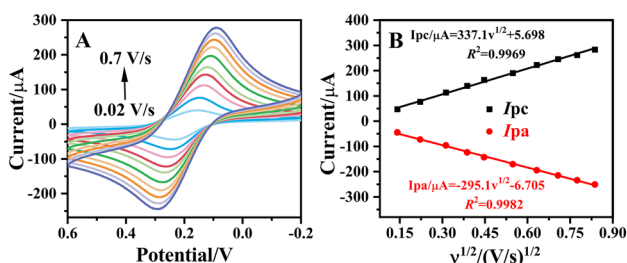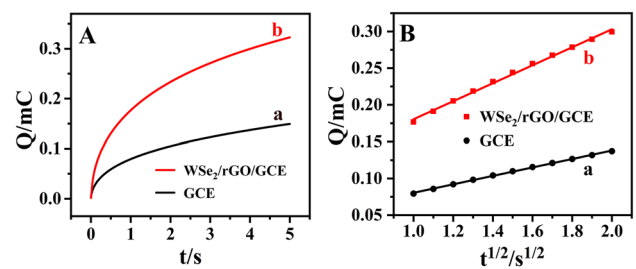

Fig. 6 Chronocoulogram (**A**) and calibration curve between Q and $t^{1/2}$ (**B**) of GCE (*a*), WSe$_2$/rGO/GCE (*b*)

the increased specific surface area of the sensing platform indicated that the flower-like WSe$_2$ and rGO here played an irreplaceable role in enhancing the effective area of the sensing interface, which may contribute to the sensitivity of the immunosensor.

Characterization of the immunosensor

To verified whether the immunosensor was constructed, DPV and CV curves at all steps were recorded. In Fig. 7A, CV curve of GCE (curve a) shows the reversible redox peaks of [Fe(CN)$_6$]$^{3-/4-}$. After rGO was immobilized (curve b) on the interface, the peak current significantly increased, which was attributed to the improvement of ECSA by rGO that can provide more active sites for the electron transfer between [Fe(CN)$_6$]$^{3-/4-}$ and the electrode. When WSe$_2$ was introduced (curve c), the peak current decreased slightly. It is probably ascribed to the semiconductor properties and steric effect of WSe$_2$. After anti-IgG (Ab) (curve d) and BSA (curve e) were absorbed onto WSe$_2$/rGO/GCE respectively,
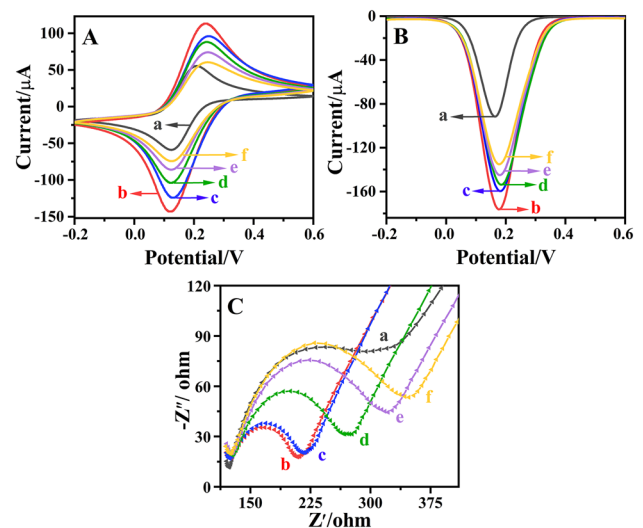

Fig. 7 The CV (**A**), DPV (**B**) and EIS (**C**) curves of immunosensor with step-by-step fabrication (*a*, GCE; *b*, rGO/GCE; *c*, WSe$_2$/rGO/GCE; *d*, Ab/WSe$_2$/rGO/GCE; *e*, BSA/Ab/WSe$_2$/rGO/GCE; *f*, Ag/BSA/Ab/WSe$_2$/rGO/GCE, hIgG concentration: 1 ng/mL)

Fig. 5 Cyclic voltammograms of WSe$_2$/rGO/GCE at different scan rates (**A**), linear dependence of peak current upon scan rates (**B**)

the peak current decreased gradually, because Ab and BSA are biomacromolecules that hinder the transfer of electrons. The hIgG (Ag) (curve f) was incubated in the last step. Anti-hIgG and hIgG formed the immune complexes, which insulated the conducting sensing interface and acted as obstructions in the electron transfer process. Therefore, CV results firmly indicated that all materials were successfully fixed on the surface of the sensing platform. As is shown in Fig. 7B, the trends of the peak current of DPV are consistent with the CV when the sensing platform was constructed layer-by-layer.

EIS measurement is a useful tool to evaluate charge transport capabilities after layer-by-layer modification. Figure 7C displayed a typical Nyquist plot, the diameter of the semicircle represents the charge transfer resistance (R_{ct}), larger diameter indicates greater charge transfer resistance on the sensing interface [43]. After the decoration of rGO, the diameter of the semicircle obviously became smaller than that of the bare GCE, indicating that R_{ct} decreased sharply. This is because rGO enlarged the electrochemical active surface area and facilitated the ion transfer. When WSe_2, Ab, BSA, Ag were immobilized in sequence respectively, the charge transfer between conductive interface and $[Fe(CN)_6]^{3-/4-}$ was blocked partly. This led to the R_{ct} growth, which was reflected in the increasement of the semicircle size. The EIS results were consistent with CV and DPV results, confirming that the WSe_2/rGO/GCE platform could achieve the goal of hIgG determination.

Optimization of experimental conditions

To achieve a higher current response and improve the accuracy in the process of analysis, the pH of PBS, the concentration of antibodies, time of the immune reaction and the temperature of immune response were optimized. All the comparisons were achieved by the peak current difference of DPV.

Antigens, antibodies and BSA were dispersed in PBS. As the activity of biomolecules will be influenced in weak acids and weak bases, pH value can be a big factor in the accuracy of the results. In Fig. 8A, the pH value is adjusted to 6.0, 6.5, 7.0, 7.5, 8.0 and 8.5, and the peak current difference were compared. It can be clearly observed that the peak current difference reached the maximum value at pH = 7.0 and decreased rapidly after that, thus 7.0 was selected as the optimal pH value.

To make full use of the active sites of the sensing interface and make sure that more antigens were captured on it, we had optimized the best concentration of antibodies. Figure 8B shows the current difference that serial concentrations (0.1 mg/mL, 0.25 mg/mL, 0.50 mg/mL, 0.75 mg/mL, 1 mg/mL) of the antibodies incubated on the sensing platform (WSe_2/rGO/GCE). The current difference rose with the
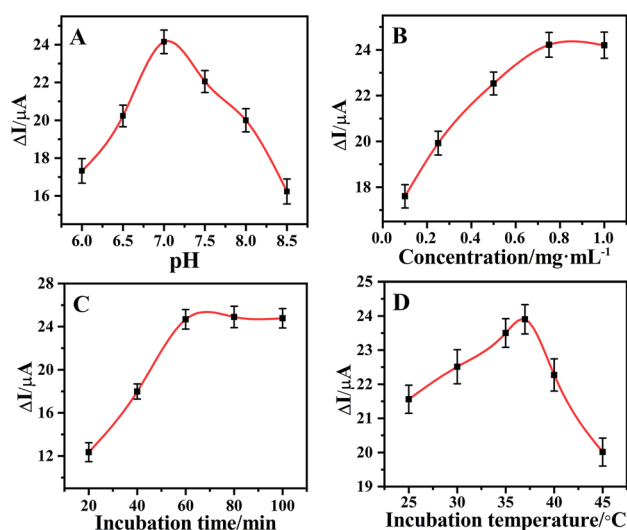

Fig. 8 Optimization of pH (**A**), concentration of antibodies (**B**), incubation time (**C**), and incubation temperature (**D**) (hIgG concentration: 10 ng/mL)

increasement of the concentrations and tended to be stable at 0.75 mg/mL, indicating that the concentration of antibodies on the electrode surface has saturated. Therefore, 0.75 mg/mL was determined as the optimal antibody concentration.

The incubation time of antigen is of great significance to the immune reaction. A robust immune-compound will form in a modest incubation time. Hence, 20, 40, 60, 80, and 100 min were set to explore the optimal incubation time. The current difference in Fig. 8C raised with the incubation time and reached the maximum at 60 min. The current difference has little significant change at 80 and 100 min, thus 60 min was chosen as the best incubation time.

Temperature is of critical significance to form stable antibody-antigen complexes. As is shown in Fig. 8D, the incubation temperature changed between 25 and 45 °C, the current difference gradually increased from 25 to 37 °C, and reached the maximum at 37 °C, and the current difference sharply decreased after that. Therefore, in the subsequent experiments, the temperature in the incubation process of antigens was set to 37 °C.

Electrochemical determination of hIgG

Calibration curves were established under the optimal experimental conditions to assess the analytical performance of the immunosensor. DPV currents at a concentration gradient were recorded in Fig. 9A. The peak current gradually decreased when the concentration of hIgG increased. It was because the large steric hindrance of immune-complex that hindered electron transport. For Fig. 9B, the linear range of the constructed immunosensor was from 0.01 to 1000 ng/mL. The fitted calibration
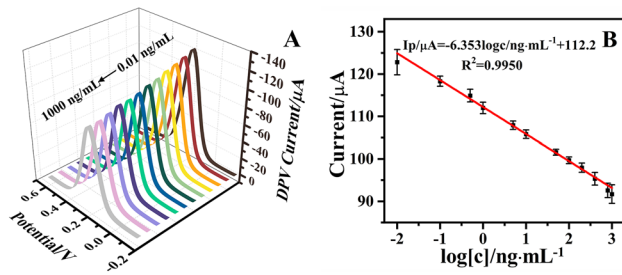
Fig. 9 Differential pulse voltammograms of Ag/BSA/Ab/WSe$_2$/rGO/GCE to 0.01–1000 ng/mL hIgG (**A**); calibration curve of the immunosensor for detecting hIgG (**B**)
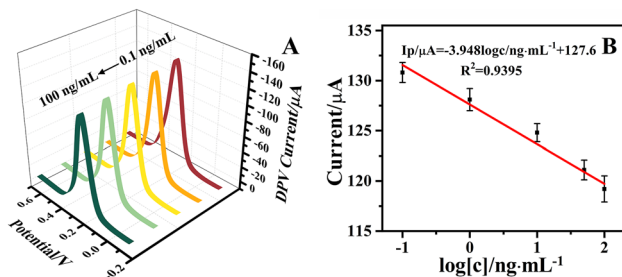

Fig. 10 Differential pulse voltammograms of Ag/BSA/Ab/rGO/GCE for different concentrations (0.1, 1.0, 10, 50, 100 ng/mL) of hIgG (**A**); calibration curve of the immunosensor for hIgG determination (**B**)

curve equation between the concentration and current was $I = -6.353\log[c] + 112.2$, with a correlation coefficient of 0.9950 and the limit of detection (LOD) was 4.72 pg/mL ($S/N = 3$).

Verification of the superiority of the WSe₂

To verify the key role of the WSe$_2$, the Ag/BSA/Ab/rGO/GCE immunosensor without the use of the WSe$_2$ was constructed. As is shown in Fig. 10A, the peak currents of the immunosensor decreased as the hIgG concentrations increased, which showed a linear correlation in the range of 0.1–100 ng/mL (Fig. 10B). The linear regression equation was $I = -3.948\log[c] + 127.6$ ($R^2 = 0.9395$), the limit of detection (LOD) was 73.3 pg/mL ($S/N = 3$). Compared to the immunosensor without WSe$_2$, the Ag/BSA/Ab/WSe$_2$/rGO/GCE immunosensor showed a wider detection range and lower detection limit. The results confirmed that the introduce of WSe$_2$ increased the loading efficiency of antibodies, which endowed the immunosensor a high sensitivity.

Comparison of immunosensor performance

As is shown in Table 1, the proposed immunosensor (WSe$_2$/rGO/GCE) exhibited a wide detection range or low detection limit when compared to other analytical methods. The results are satisfying, demonstrating that the immunosensor has a promising ability for quantifying hIgG. The high performance mainly benefited from WSe$_2$ with large surface area that can vastly promoting the amounts of antibodies. Besides, the high current response that profit from rGO can provide a high current signal that broaden the detection range.

Specificity, reproducibility, and stability of the immunosensor

To evaluate the specificity of the proposed immunosensor, the sensing interface (BSA/Ab/WSe$_2$/rGO/GCE) was added with 10 ng/mL hIgG, 100 ng/mL interfering substances

Table 1 Comparisons of different methods to detect human IgG

Substrate	Substrate materials/label materials	Detection method	Linear rage (ng/mL)	LOD (ng/mL)	References
LAG	PAAMI/Pt-NPs-anti-IgG	DPV	0.012–352	6.0×10^{-3}	[44]
GCE	BSA/PANI-NWs-aptamer	DPV	1–10,000	0.27	[45]
SPCE	P2ABA-anti-IgG	DPV	1–50	0.15	[46]
SPCE	Cu(II)/GO-anti-IgG	SWV	0.001–0.5	2.0×10^{-4}	[47]
GE	β-Cyclodextrin/Fc-IL-CHO-anti-IgG	EIS	0.1–50	0.03	[48]
GCE	IgG-MIH	EIS	0.5–200	0.03	[49]
GCE	Ru(bpy)$_3^{2+}$/AuNPs-anti-IgG	ECL	0.01–10	5×10^{-3}	[50]
		LFIA	4.6–100	0.72	[12]
		ELISA	200–15,000	30	[51]
GCE	rGO/WSe$_2$-anti-hIgG	DPV	0.01–1000	4.72×10^{-3}	This work

LAG laser-ablated graphene, *GCE* glassy carbon electrode, *SPCE* screen-printed carbon electrodes, *GE* gold electrode, *IgG-MIHs* IgG imprinted hydrogels, *DPV* differential pulse voltammetry, *SWV* square wave voltammetry, *EIS* electrochemical impedance spectra, *ECL* electrochemiluminescence, *LFIA* Lateral Flow Immunoassay, *ELISA* enzyme-linked immuno-sorbent assay
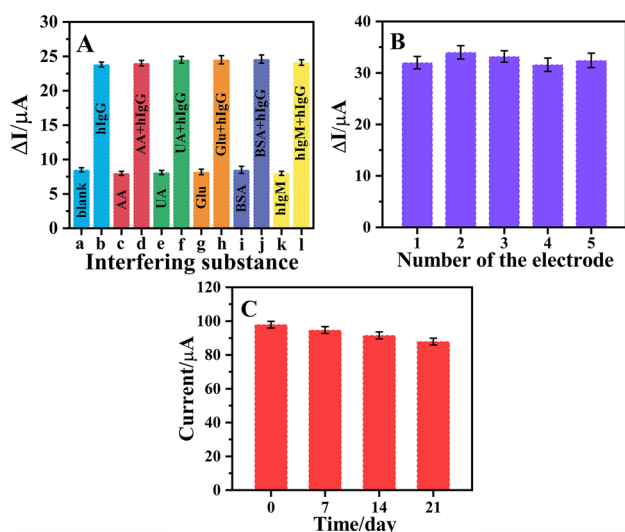
Fig. 11 Selectivity of the immunosensor using 10 ng/mL hIgG and 100 ng/mL interferences (**A**); reproducibility (**B**) and stability (**C**) of the immunosensor under the presence of 100 ng/mL hIgG

Real sample analysis

The real sample analysis is a critical part in evaluating the feasibility of the proposed immunosensor in clinical applications. Hence, the spike recovery test was carried out to measure the hIgG concentrations in several human serum samples [52]. First, the blood samples obtained from the hospital were centrifuged and diluted with PBS. As a standard reference, hIgG concentrations in diluted serum samples were tested using a commercial ELISA kit. Second, the diluted serum samples were dropped onto the interfaces of the immunosensor to obtain the peak current of DPV. Third, a certain concentration of standard hIgG sample was added into several serum samples and was diluted to perform the test again. The concentrations of hIgG were obtained, and spiked recovery rates were calculated using the above results. As is shown in Table 2, the average contents of hIgG in human serum measured by immunosensor are agree well with that were tested by ELISA kit. The recovery rates are between 95.5% and 104.1%, and the relative standard deviations are between 0.8% and 2.5%. These results are acceptable and satisfying. Therefore, the immunosensor has great potential in clinical determination of hIgG.

including ascorbic acid (AA), uric acid (UA), glucose (Glu), BSA, hIgM. And each of them was mixed with 10 ng/mL hIgG respectively to compare the DPV peak current differences. The results in Fig. 11A showed that the current difference of the interferent substances and blank group were extremely close. While the immunosensor containing target and 10 times of interferent had approximate current differences with the immunosensor that only containing hIgG. These results indicated that the proposed sensing platform has favorable selectivity and anti-interference ability.

Same modification processes were established on five different immunosensors to verified the reproducibility of the immunosensor. Figure 11B compares the current difference of 5 different electrodes. The relative standard deviations (RSDs) among them are below 5%, indicating that the immunosensor has excellent reproducibility.

The stability of the immunosensor is an indispensable character to evaluate its practical potential. The prepared immunosensor was dropped with 100 ng/mL hIgG and was placed in a 4 °C refrigerator. The measurement was carried out every week to record the signal of DPV. The results are shown in Fig. 11C. After 7 days of storage, the peak current decreased by only 3.23%. Moreover, the peak current decreased by 6.48% and 10.17% after 14 and 21 days of storage respectively. The degree of current decrease was acceptable, revealing the satisfactory stability of the immunosensor.

Conclusion

In this study, the flower-like WSe_2 acted as a bio-matrix, and cooperated with rGO to form a high-performance sensing interface that can sensitively analyze hIgG. Taking full advantages of the porous structure and large specific surface area of the WSe_2, large amounts of antibodies were fixed on the sensing interface. Meanwhile, rGO with high electroactivity drastically improved the current signal. Therefore, with the combination of WSe_2 and rGO, the sensitivity of the immunosensor was greatly improved, displaying a wide linear range from 0.01 to 1000 ng/mL and a low detection limit of 4.72 pg/mL for hIgG determination. Furthermore, the sensing platform exhibited great analytical performance including the stability, specificity and reproducibility. Therefore, this study has proposed an effective way to apply WSe_2 in establishing sensing platform for clinical hIgG determination. This will provide an effective reference for the followup research about WSe_2 and other transition metal dichalcogenides in biosensing filed.

Table 2 Recovery tests of hIgG in real samples

Sample	ELISA (mg/mL)	RSD (%, $n = 5$)	Immu-nosensor (mg/mL)	Added (mg/mL)	Total with standard addition (mg/mL)	Average (mg/mL)	RSD (%, $n = 5$)	Recoveries (%)
1	5.74	2.1	6.06	10.00	15.13, 15.88, 15.60 16.20, 15.71	15.70	2.5	96.4
2	8.89	2.99	9.58	10.00	19.13, 19.53, 19.01, 18.70, 19.26	19.13	1.6	95.5
3	14.16	3.32	14.47	10.00	24.40, 24.98, 24.33 25.53, 25.15	24.88	2.05	104.1
4	16.87	3.9	17.13	20.00	37.09, 36.50, 36.67 37.02, 37.19	36.89	0.8	98.8
5	23.01	2.62	22.70	20.00	41.81, 42.65, 44.12 44.23, 43.58	43.28	2.38	102.9

Declarations

Conflicts of interest On behalf of all authors, the corresponding author states that there is no conflict of interest.

References

1. A.R. Duncan, G.J.N. Winter, The binding site for C1q on IgG. Nature **332**, 738–740 (1988)
2. S.L. Caddy, M. Vaysburd, M. Wing, S. Foss, J.T. Andersen, K. O'Connell, K. Mayes, K. Higginson, M. Iturriza-Gómara, U. Desselberger et al., Intracellular neutralisation of rotavirus by VP6-specific IgG. PLoS Pathog. **16**, e1008732 (2020)
3. S. Kdimati, C.S. Mullins, M. Linnebacher, Cancer-cell-derived IgG and its potential role in tumordevelopment. Int. J. Mol. Sci. **22**, 11597 (2021)
4. D.C. Roopenian, S. Akilesh, FcRn: the neonatal Fc receptor comes of age. Nat. Rev. Immunol. **7**, 715–725 (2007)
5. A. Gonzalez-Quintela, R. Alende, F. Gude, J. Campos, J. Rey, L.M. Meijide, C. Fernandez-Merino, C. Vidal, Serum levels of immunoglobulins (IgG, IgA, IgM) in a general adult population and their relationship with alcohol consumption, smoking and common metabolic abnormalities. Clin. Exp. Immunol. **151**, 42–50 (2008)
6. G. Wang, H. Li, J. Pan, T. Yan, H. Zhou, X. Han, L. Su, L. Hou, X. Xue, Upregulated expression of cancer-derived immunoglobulin G is associated with progression in glioma. Front Oncol. **11**, 758856 (2021)
7. M.A. De Roza, M. Lamba, G.B.B. Goh, J.H.M. Lum, M.C.C. Cheah, J.H.J. Ngu, Immunoglobulin G in non-alcoholic steatohepatitis predicts clinical outcome: a prospective multi-centre cohort study. World J. Gastroenterol. **27**, 7563 (2021)
8. Q. Zhang, L. Xiang, M.H. Zaman, W. Dong, G. He, G.M. Deng, Predominant role of immunoglobulin G in the pathogenesis of splenomegaly in murine lupus. Front Immunol. **10**, 3020 (2019)
9. R. Lin, H. Chen, W. Shu, M. Sun, L. Fang, Y. Shi, Z. Pang, W. Wu, Z. Liu, Clinical significance of soluble immunoglobulins A and G and their coated bacteria in feces of patients with inflammatory bowel disease. J. Transl. Med. **16**, 359 (2018)
10. W. Lu, P. Wu, L. He, Y. Meng, P. Wu, W. Ding, J. Liu, Dynamic antibody responses in patients with different severity of COVID-19: a retrospective study. Infect Dis. Ther. **10**, 1379–1390 (2021)
11. J. Akimoto, H. Kashiwagi, N. Morishima, S. Obuse, T. Isoshima, T. Kageyama, H. Nakajima, Y. Ito, Rapid and quantitative detection of multiple antibodies against SARS-CoV-2 mutant proteins by photo-immobilized microarray. Anal. Sci. **38**, 1313–1321 (2022)
12. Y. Tang, H. Gao, F. Kurth, L. Burr, K. Petropoulos, D. Migliorelli, O.T. Guenat, S. Generelli, Nanocellulose aerogel inserts for quantitative lateral flow immunoassays. Biosens. Bioelectron. **192**, 113491 (2021)
13. X. Tan, M. Krel, E. Dolgov, S. Park, X. Li, W. Wu, Y.L. Sun, J. Zhang, M.K. Khaing Oo, D.S. Perlin et al., Rapid and quantitative detection of SARS-CoV-2 specific IgG for convalescent serum evaluation. Biosens. Bioelectron. **169**, 112572 (2020)
14. J.-T. Cao, X.-M. Liu, Y.-Z. Fu, S.-W. Ren, Y.-M. Liu, Label-free ratiometric electrochemiluminescent (ECL) immunosensor for the determination of prostate specific antigen (PSA) in Serum. Anal. Lett. **55**, 1810–1821 (2022)
15. Z. Yin, C. Liu, Y. Yi, H. Wu, X. Fu, Y. Yan, A label-free electrochemical immunosensor based on PdPtCu@BP bilayer nanosheets for point-of-care kidney injury molecule-1 testing. J. Electroanal. Chem. **917**, 116420 (2022)
16. V. Podzorov, M.E. Gershenson, C. Kloc, R. Zeis, E. Bucher, High-mobility field-effect transistors based on transition metal dichalcogenides. Appl. Phys. Lett. **84**, 3301–3303 (2004)
17. K.S. Novoselov, D. Jiang, F. Schedin, T.J. Booth, V.V. Khotkevich, S.V. Morozov, A.K. Geim, Two-dimensional atomic crystals. Proc. Natl. Acad. Sci. USA. **102**, 10451–10453 (2005)

18. X. Yu, M.S. Prevot, N. Guijarro, K. Sivula, Self-assembled 2D WSe_2 thin films for photoelectrochemical hydrogen production. Nat. Commun. **6**, 7596 (2015)

19. Z. Ma, P. Konze, M. Küpers, K. Wiemer, D. Hoffzimmer, S. Neumann, S. Kunz, U. Simon, R. Dronskowski, A. Slabon, Elucidation of the active sites for monodisperse FePt and Pt nanocrystal catalysts for p-WSe_2 photocathodes. J. Phys. Chem. C **124**, 11877–11885 (2020)

20. I.-T. Cho, J.I. Kim, Y. Hong, J. Roh, H. Shin, G.W. Baek, C. Lee, B.H. Hong, S.H. Jin, J.-H. Lee, Low frequency noise characteristics in multilayer WSe_2 field effect transistor. Appl. Phys. Lett. **106**, 023504 (2015)

21. D. Vikraman, A.A. Arbab, S. Hussain, N.K. Shrestha, S.H. Jeong, J. Jung, S.A. Patil, H.-S. Kim, Design of WSe_2/MoS_2 heterostructures as the counter electrode to replace Pt for dye-sensitized solar cell. ACS Sustain. Chem. Eng. **7**, 13195–13205 (2019)

22. P. Fathi-Hafshejani, N. Azam, L. Wang, M.A. Kuroda, M.C. Hamilton, S. Hasim, M. Mahjouri-Samani, Two-dimensional-material-based field-effect transistor biosensor for detecting COVID-19 virus (SARS-CoV-2). ACS Nano **15**, 11461–11469 (2021)

23. M.M. Rahman, L.F. Abdulrazak, M. Ahsan, M.A. Based, M.M. Rana, M.S. Anower, K.A. Rikta, J. Haider, S. Gurusamy, 2D nanomaterial-based hybrid structured (Au-WSe_2-$PtSe_2$-BP) surface plasmon resonance (SPR) sensor with improved performance. IEEE Access **10**, 689–698 (2022)

24. H.W. Lee, D.H. Kang, J.H. Cho, S. Lee, D.H. Jun, J.H. Park, Highly sensitive and reusable membraneless field-effect transistor (FET)-type Tungsten diselenide (WSe_2) Biosensors. ACS Appl. Mater. Interfaces **10**, 17639–17645 (2018)

25. Y.H. Wang, H. Xia, K.J. Huang, X. Wu, Y.Y. Ma, R. Deng, Y.F. Lu, Z.W. Han, Ultrasensitive determination of thrombin by using an electrode modified with WSe_2 and gold nanoparticles, aptamer-thrombin-aptamer sandwiching, redox cycling, and signal enhancement by alkaline phosphatase. Mikrochim Acta **185**, 502 (2018)

26. H. Kaur, M. Shorie, P. Sabherwal, Biolayer interferometry-SELEX for Shiga toxin antigenic-peptide aptamers & detection via chitosan-WSe_2 aptasensor. Biosens. Bioelectron. **167**, 112498 (2020)

27. V. Georgakilas, J.N. Tiwari, K.C. Kemp, J.A. Perman, A.B. Bourlinos, K.S. Kim, R. Zboril, Noncovalent functionalization of graphene and graphene oxide for energy materials, biosensing, catalytic, and biomedical applications. Chem. Rev. **116**, 5464–5519 (2016)

28. Y. Luo, L. Shi, H. He, G. Yang, G. Cong, C. Zhu, J.J.C. Xu, Vertical growth of nickel sulfide nanosheets on graphene oxide for advanced sodium-ion storage. Carbon **182**, 194–202 (2021)

29. P. Hampitak, T.A. Jowitt, D. Melendrez, M. Fresquet, P. Hamilton, M. Iliut, K. Nie, B. Spencer, R. Lennon, A. Vijayaraghavan, A point-of-care immunosensor based on a quartz crystal microbalance with graphene biointerface for antibody assay. ACS Sens. **5**, 3520–3532 (2020)

30. R. Ji, W. Niu, S. Chen, W. Xu, X. Ji, L. Yuan, H. Zhao, M. Geng, J. Qiu, C. Li, Target-inspired Pb^{2+}-dependent DNAzyme for ultrasensitive electrochemical sensor based on MoS_2-AuPt nanocomposites and hemin/G-quadruplex DNAzyme as signal amplifier. Biosens. Bioelectron. **144**, 111560 (2019)

31. S.S. Yoo, S.Y. Kim, K.S. Kim, S. Hong, M.J. Oh, M.G. Nam, W.-J. Kim, J. Park, C.-H. Chung, W.-S. Choe et al., Controlling inter-sheet-distance in reduced graphene oxide electrodes for highly sensitive electrochemical impedimetric sensing of myoglobin. Sens. Actuat. B: Chem. **305**, 127477 (2020)

32. P. Kanagavalli, C. Andrew, M. Veerapandian, M. Jayakumar, In-situ redox-active hybrid graphene platform for label-free electrochemical biosensor: Insights from electrodeposition and electroless deposition. TrAC, Trends Anal. Chem. **143**, 116413 (2021)

33. W.S. Hummers Jr., R.E. Offeman, Preparation of graphitic oxide. J. Am. Chem. Soc. **80**, 1339–1339 (1958)

34. Y. Lei, Z. Tang, R. Liao, B. Guo, Hydrolysable tannin as environmentally friendly reducer and stabilizer for graphene oxide. Green Chem. **13**, 1655 (2011)

35. B. Yu, B. Zheng, X. Wang, F. Qi, J. He, W. Zhang, Y. Chen, Enhanced photocatalytic properties of graphene modified few-layered WSe_2 nanosheets. Appl. Surf. Sci. **400**, 420–425 (2017)

36. J. Shen, T. Li, Y. Long, M. Shi, N. Li, M. Ye, One-step solid state preparation of reduced graphene oxide. Carbon **50**, 2134–2140 (2012)

37. X. Peng, Z. Wang, Z. Wang, J. Gong, H. Hao, Electron reduction for the preparation of rGO with high electrochemical activity. Catal. Today **337**, 63–68 (2019)

38. J. Xu, Z. Wei, S. Zhang, X. Wang, Y. Wang, M. He, K. Huang, Hierarchical WSe_2 nanoflower as a cathode material for rechargeable Mg-ion batteries. J. Colloid Interface **588**, 378–383 (2021)

39. X. Wang, Y. Chen, B. Zheng, F. Qi, J. He, Q. Li, P. Li, W. Zhang, Graphene-like WSe_2 nanosheets for efficient and stable hydrogen evolution. J. Alloy. Compd. **691**, 698–704 (2017)

40. M. Muska, J. Yang, Y. Sun, J. Wang, Y. Wang, Q. Yang, $CoSe_2$ nanoparticles dispersed in WSe_2 nanosheets for efficient electrocatalysis and supercapacitance applications. ACS Appl. Nano Mater. **4**, 5796–5807 (2021)

41. D.A. Aikens, Electrochemical methods, fundamentals and applications. J. Chem. Educ. **60**, A25 (1983)

42. F.J.A.C. Anson, Application of potentiostatic current integration to the study of the adsorption of cobalt (III)-(Ethylenedinitrilo (tetraacetate) on mercury electrodes. Anal. Chem. **36**, 932–934 (1964)

43. T. Matsubara, M. Ujie, T. Yamamoto, Y. Einaga, T. Daidoji, T. Nakaya, T. Sato, Avian influenza virus detection by optimized peptide termination on a boron-doped diamond electrode. ACS Sens. **5**, 431–439 (2020)

44. S.C. Barman, M.A. Zahed, M. Sharifuzzaman, S.G. Ko, H. Yoon, J.S. Nah, X. Xuan, J.Y. Park, A polyallylamine anchored amine-rich laser-ablated graphene platform for facile and highly selective electrochemical IgG biomarker detection. Adv. Func. Mater. **30**, 1907297 (2020)

45. Y. Li, R. Han, M. Chen, L. Zhang, G. Wang, X. Luo, Bovine serum albumin-cross-linked polyaniline nanowires for ultralow fouling and highly sensitive electrochemical protein quantification in human serum samples. Anal. Chem. **93**, 4326–4333 (2021)

46. T. Putnin, W. Jumpathong, R. Laocharoensuk, J. Jakmunee, K. Ounnunkad, A sensitive electrochemical immunosensor based on poly(2-aminobenzylamine) film modified screen-printed carbon electrode for label-free detection of human immunoglobulin G. Artif. Cells Nanomed. Biotechnol. **46**, 1042–1051 (2018)

47. S. Phetsang, D. Khwannimit, P. Rattanakit, P. Chanlek, P. Kidkhunthod, P. Mungkornasawakul, J. Jakmunee, K. Ounnunkad, A redox Cu(II)-graphene oxide modified screen printed carbon electrode as a cost-effective and versatile sensing platform for electrochemical label-free immunosensor and non-enzymatic glucose sensor. Front. Chem. **9**, 671173 (2021)

48. Y. Shen, G. Shen, Electrochemical impedimetric immunosensor based on host–guest interaction between β-cyclodextrin and ferrocene anchored to ionic liquid. Ionics **25**, 3407–3412 (2019)

49. M. Cui, Y. Gong, M. Du, K. Wang, T. Li, X. Zhu, S. Wang, X. Luo, An antifouling electrochemical biosensor based on a protein imprinted hydrogel for human immunoglobulin G recognition in complex biological media. Sens. Actuat. B Chem. **337**, 129820 (2021)

50. C. Zhao, L. Niu, X. Wang, W. Sun, A simple and convenient electrochemiluminescence immunoassay by using gold nanoparticles

Flower-like WSe₂ used as bio-matrix in ultrasensitive label-free electrochemical...

1403

as both label and co-reactant. Bioelectrochemistry **135**, 107585 (2020)

51. M.M. Neumann, D. Volodkin, Porous antibody-containing protein microparticles as novel carriers for ELISA. Analyst **145**, 1202–1206 (2020)

52. B.E. Saxberg, B.R. Kowalski, Generalized standard addition method. Anal. Chem. **51**, 1031–1038 (1979)